

First-principles analysis of the effect of magnetic states on the oxygen vacancy formation energy in doped $\text{La}_{0.5}\text{Sr}_{0.5}\text{CoO}_3$ perovskite

Wei Wei,* Florian Fuchs, Andreas Zienert, Xiao Hu, and Jörg Schuster

Center for Microtechnologies, Chemnitz University of Technology, Chemnitz 09107 Saxony, Germany and
Fraunhofer Institute for Electronic Nano Systems, Chemnitz 09126 Saxony, Germany

(Dated: July 11, 2025)

Oxygen vacancies are critical for determining the electrochemical performance of fast oxygen ion conductors. The perovskite $\text{La}_{0.5}\text{Sr}_{0.5}\text{CoO}_3$, known for its excellent mixed ionic-electronic conduction, has attracted significant attention due to its favorable vacancy characteristics. In this study, we employ first-principles calculations to systematically investigate the impact of $3d$ transition-metal doping on the oxygen vacancy formation energies in the perovskite. Two magnetic states, namely the ferromagnetic and paramagnetic states, are considered in our models to capture the influence of magnetic effects on oxygen vacancy energetics. Our results reveal that the oxygen vacancy formation energies are strongly dependent on both the dopant species and the magnetic state. Notably, the magnetic states alter the vacancy formation energy in a dopant-specific manner due to double exchange interactions, indicating that relying solely on the ferromagnetic ground state may result in misleading trends in doping behavior. These findings emphasise the importance of accounting for magnetic effects when investigating oxygen vacancy properties in perovskite oxides.

I. INTRODUCTION

Defect-driven transport phenomena are fundamental to the operation of fast ion-conducting solid electrodes and electrolytes [1]. During operation, intrinsic or extrinsic defects serve as the primary pathways for ionic migration. Among these defects, the critical role of oxygen vacancies extends to a broad class of fast-ion conductors, where their presence and mobility directly impact the efficiency of oxygen-ion transport [2, 3]. Materials that accommodate high concentrations of oxygen vacancies, such as fluorite and perovskite crystals, often exhibit enhanced ionic conductivity and redox behavior, which are vital for applications including solid oxide fuel cells (SOFCs) and oxygen separation membranes [4, 5]. Within this context, perovskite crystals have garnered significant attention due to their tunable defect chemistry and fast oxygen-ion conduction.

The perovskite framework, namely the compound of ABO_3 , exhibits enhanced flexibility among the family of metal oxides [6]. This superior adaptability facilitates a broader range of ionic substitutions and the accommodation of various structural defects. Among them, the cobalt-based perovskites are a prominent category due to their exceptional oxygen diffusivity and oxygen surface exchange coefficient [7]. Various studies of A-position and B-position occupants have been added to such materials to accommodate a wide range of operating conditions. The inherent tunability of their B-site cation allows for precise engineering of oxygen vacancy formation and ionic transport properties [8]. For instance, partial substitution of Co with other transition metal (TM) elements has been extensively explored to enhance stability under operational conditions or optimize ionic conductivity [9].

Despite these advances, open questions remain concerning the interplay between dopant chemistry and oxygen vacancy behavior, particularly under different manufacturing methods. Previous experimental studies have developed strategies such as nanostructuring, surface modification, and composite designs to improve the oxygen reduction reaction activity and durability of perovskite cathodes [10, 11]. However, these methods frequently depend on the synergistic effect of multiple factors, resulting in the potential for contradictory outcomes for the same dopant elements. For example, Cheng *et al.* reported that Fe doping increases the concentration of lattice oxygen vacancies, thereby enhancing the performance of $\text{La}_{1-x}\text{Sr}_x\text{CoO}_{3-\delta}$ [12]. In contrast, Mantzavinos *et al.* observed that increasing Fe content leads to a decrease in oxygen vacancy concentration [13]. Consequently, theoretical calculations have been sought to elucidate the intrinsic effect of doping elements on the nature of oxygen vacancies in the perovskite [14].

Extensive theoretical studies have been conducted to investigate oxygen vacancy formation in cobalt-based perovskites [14–16]. However, these studies often focus on single-element doping effects and assume an idealized ferromagnetic (FM) ground state, neglecting the paramagnetic (PM) states that prevail at elevated temperatures during device operation [11]. This oversight limits the predictive accuracy and rationality of computational models. For instance, Jia *et al.* demonstrated that Fe doping of cobalt-based perovskites decreases oxygen vacancy formation energy in the PM state [17]. This variation underscores the necessity of incorporating both magnetic states into theoretical investigations to accurately predict dopants behavior in operational environments.

In this work, we systematically investigate the impact of substituting Co with Mn, Fe, Ni, and Cu on the energetics of oxygen vacancy formation in $\text{La}_{0.5}\text{Sr}_{0.5}\text{CoO}_3$ (LSC), considering both FM and PM states. Using density functional theory (DFT), we evaluate the interplay

* wei.wei@enas.fraunhofer.de

among dopant electronic configurations, magnetic order/disorder, and oxygen vacancy stability. These findings provide key insights for designing next-generation perovskite SOFC cathodes with tailored oxygen vacancy concentrations and enhanced electrochemical performance.

The paper is organized as follows: In Sec. II we introduce the computational setup and the definition of the formation energy of oxygen vacancies in LSC. In Sec. III, we present the results on stability of oxygen vacancies by different magnetic states, and its influence on the electronic structure. In Sec. IV, we discuss our results in view of other findings in the literature, and we summarize and conclude in Sec. V.

II. THEORETICAL APPROACH

A. Crystal structure of LSC

In earlier studies, the parent LSC phase was considered to adopt a cubic perovskite structure (space group $Pm\bar{3}m$) under operating conditions and room temperature [18, 19]. The structure consists of corner-sharing $\text{CoO}_6^{2/3-}$ octahedra, with La^{3+} and Sr^{2+} ions randomly occupying the A-site, creating a disordered cationic sublattice. Investigations on similar perovskites have further revealed that the energies associated with different La/Sr configurations are very close, allowing the use of isotropic supercells to reliably capture the average structural and electronic properties of these materials [20, 21]. A perfect cubic model with an ordered La/Sr configuration is depicted in Figure 1a. The lattice constant of this cubic model is 3.85 Å by DFT, which is in good agreement with the experimental values of 3.83 Å [22, 23]. However, more recent studies indicate that under operating conditions, particularly in thin films, LSC does not maintain a perfect cubic symmetry but rather exhibits a pseudo-cubic structure characterized by distortions in the Co-O octahedra [15, 24, 25].

The pseudo-cubic structure of LSC with distorted Co-O octahedra can be mainly attributed to the Jahn-Teller (J-T) effect [26]. The J-T effect arises from electronic degeneracies in the Co d orbitals, which drive a spontaneous symmetry breaking in the CoO_6 octahedra to lower the energy of the system [27, 28]. Such structural modifications not only alter the local lattice geometry but also have profound implications on the electronic structure and oxygen vacancy formation energetics, thereby influencing the electrochemical performance of the material [29]. Therefore, we have incorporated the structural distortion into our model, as illustrated in Figure 1b.

In our models, we replace one of the Co atoms with the aforementioned TM elements. At such low doping concentrations, the crystal retains its pseudo-cubic structure, and the lattice constant does not change significantly [30]. Therefore, we use the same size of the simulation box for all the models.

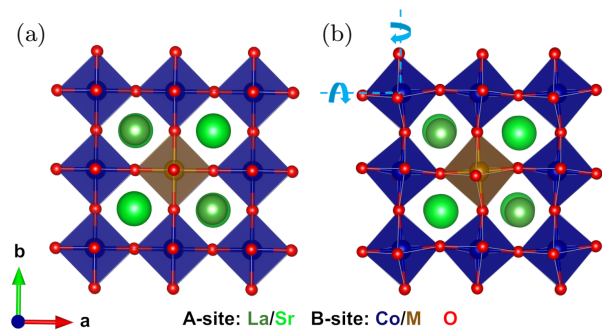


FIG. 1: Atomic structures of doped LSC. (a) The ordered perovskite structure with the dopant M substituting for Co at a B-site. (b) The distorted structure induced by the J-T effect. The light blue arrows indicate the rotation of the B-O octahedra. La/Sr atoms are shown in dark/light green, Co atoms in blue, O atoms in red, and the dopant site by M is marked in dark gold.

B. Magnetic order calculations

The magnetic properties of LSC are governed by the complex interplay between $\text{Co}^{3+}/\text{Co}^{4+}$ spin states and oxygen vacancy distributions [31]. At temperatures lower than 250 K, LSC exhibits FM ordering due to double exchange between two Co ions through the intermediate shared O atom [18, 19]. However, at most operating temperatures, thermal fluctuations disrupt the long-range FM order, leading to a PM state with short-range spin correlations [31].

Simulating the exact noncollinear magnetic configurations in the PM state is computationally expensive due to the size of the supercell and the need for extensive statistical sampling. Instead, we employ the Magnetic Sampling Method (MSM) [32], which simulates PM states using the average of a certain amount of collinear magnetic configurations, as shown in Figure 2. In each of the samples, the total magnetic moment is set to 0 μ_B . The MSM approach has been validated against more rigorous methods (e.g., DLM-CPA) for transition metal oxides, yielding comparable accuracy in predicting magnetic and electronic properties [32].

In this work, the MSM implementation involves generating 20 distinct collinear spin configurations for our models. This approach captures the essential physics of the PM state while maintaining computational feasibility, as demonstrated by its successful application to similar transition metal oxides systems [33–35].

C. Computational details

The calculations are carried out with the Vienna ab initio simulation package [36] employing projector-augmented waves [37] and the spin-polarized Perdew-Burke-Ernzerhof [38] generalized gradient approxima-

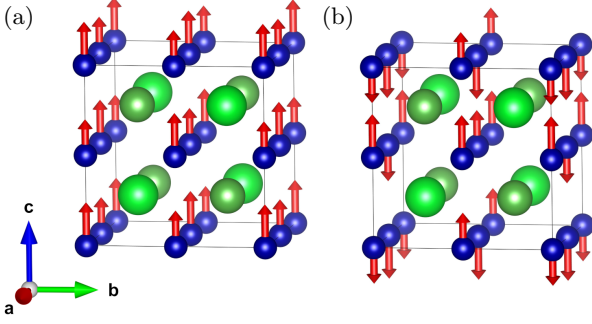


FIG. 2: Magnetic configurations of LSC: (a) the FM state, and (b) one of the PM state configurations. The magnetic moments of TM elements are represented by red arrows. To improve clarity, oxygen atoms are not shown.

tion. The interaction between valence electrons and ionic cores is modeled by treating the $5s$, $5p$, and $6s$ orbitals of La, the $4s$, $4p$, and $5s$ orbitals of Sr, the $3s$, $3p$, $3d$, and $4s$ orbitals of TM elements, and the $2s$ and $2p$ orbitals of O as valence electrons. To avoid the self-interaction errors that occur in the standard DFT for strongly correlated electronic systems, we employ the DFT+U method [39] accounting for the on-site Coulomb interaction in the localized d orbital.

In our calculations, an energy cutoff of 600 eV is used for the plane-wave basis. Total energy differences and forces on atoms for all structural degrees of freedom are converged within 1×10^{-5} eV and 5×10^{-2} eV/Å, respectively. The Brillouin-zone integrals are sampled by $4 \times 4 \times 4$ Monkhorst-Pack k -point grids [40] with a Gaussian smearing of 1×10^{-3} eV for the $2 \times 2 \times 2$ supercell models containing 40 atoms with composition $\text{La}_{0.5}\text{Sr}_{0.5}\text{Co}_{0.875}\text{M}_{0.125}\text{O}_3$ ($M = \text{Mn, Fe, Co, Ni, Cu}$). Structural relaxations for these systems are carried out using the Fast Inertial Relaxation Engine (FIRE) algorithm [41]. The specific U values employed are 4.0 eV for Mn, Cu and Fe, 3.3 eV for Co, and 6.4 eV for Ni [42]. Defect formation energies of TM dopants located at B sites in the perovskite crystal are calculated as

$$E_{\text{TM}}^{\text{doping}} = \frac{E_{(\text{La/Sr})\text{Co}_{1-y}\text{M}_y\text{O}_3} - E_{\text{LSC}}^{\text{bulk}} - y(E_{\text{M}}^{\text{metal}} + E_{\text{Co}}^{\text{metal}})}{y} \quad (1)$$

where $E_{(\text{La/Sr})\text{Co}_{1-y}\text{M}_y\text{O}_3}$ is the total energy per formula unit of the doped perovskite crystal, $E_{\text{LSC}}^{\text{bulk}}$ is the energy per formula unit of the pure LSC reference crystal, $E_{\text{M}}^{\text{metal}}$ and $E_{\text{Co}}^{\text{metal}}$ are the energy per atom in the most stable phase of the elemental metals, and y is the proportion of dopant per formula unit of the perovskite crystal.

Similarly, the formation energy of an oxygen vacancy in the perovskite crystal is calculated as

$$E_{\text{V}}^{\text{O}} = E_{\text{sys}}^{\text{vac}} - E_{\text{sys}}^{\text{bulk}} + \frac{1}{2}E_{\text{O}_2} \quad (2)$$

where $E_{\text{sys}}^{\text{vac}}$ is the total energy of the (doped or non-

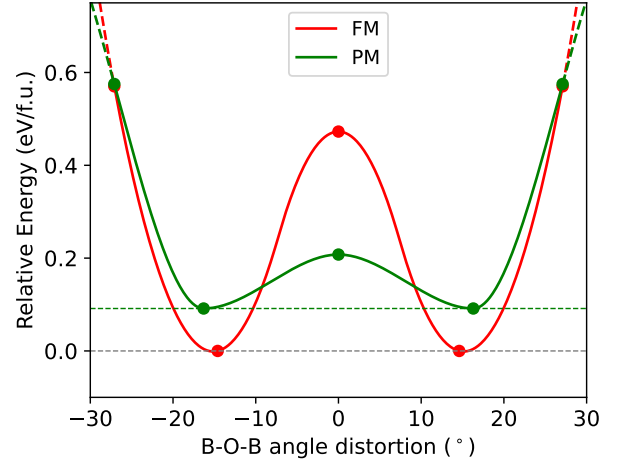


FIG. 3: Relative energy per formula unit as a function of B-O-B angle distortion in LSC for FM (red) and PM (green) configurations. The cubic structure corresponds to the local energy maximum at 0° distortion, indicating its instability due to the Jahn-Teller effect. All energies are referenced to the lowest energy point in the FM configuration, marked as 0 eV on the vertical axis.

doped) perovskite crystal with an oxygen vacancy, $E_{\text{sys}}^{\text{bulk}}$ is the total energy of the same crystal without oxygen vacancies, and E_{O_2} is the energy of an oxygen molecule. In our calculations, we consider a single oxygen vacancy by removing one O atom from a total of 24 O atoms in our model.

III. RESULTS

A. Structural distortion of LSC

To elucidate the energy landscape associated with distortions of CoO_6 octahedra in LSC, we investigated the relative energy as a function of the B-O-B bond angle distortion. The J-T effect plays a crucial role in the distortions, leading to the instability of the ordered cubic structure, which manifests as a saddle point in the potential energy surface. As demonstrated in Figure 3, we compared the potential energy surface of two distinct magnetic configurations: FM and PM states. In our results, all energies are referenced to the lowest energy point in the FM configuration, which is set to 0 eV. The energy profiles exhibit a characteristic double-well potential, with minima corresponding to distorted structures and a local energy maximum at the undistorted cubic phase (0° distortion). Deviations from 0° represent increasing distortion, with positive and negative angles indicating different distortion directions.

The stability of different magnetic configurations varies with structural distortions. The FM configuration exhibits its minimum energy at a distorted angle of $\pm 15^\circ$.

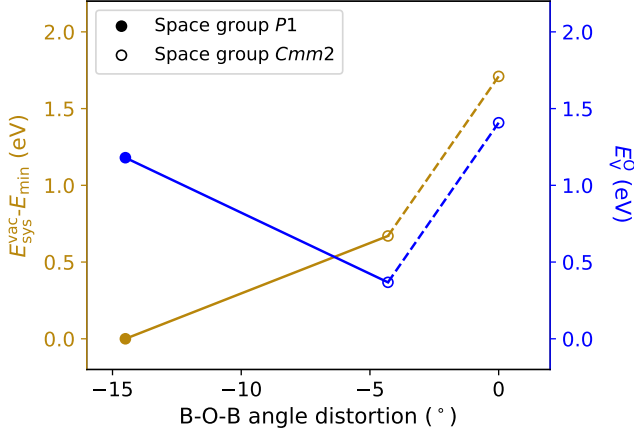


FIG. 4: Energy analysis of vacancy-containing LSC structures as a function of B-O-B angle distortion. The dark yellow curve represents the total system energy $E_{\text{vac}}^{\text{vac}}$, referenced to the lowest energy configuration E_{min} . The blue curve shows the oxygen vacancy formation energy E_v^O . The solid and open markers indicate different symmetry of the crystal.

While, the PM configuration shows a higher energy minimum at a similar distortion angle, which is $\pm 16^\circ$, with an energy difference of 0.09 eV per formula unit relative to the FM state. At the 0° distortion, the PM state is more stable than the FM state, with the PM energy being 0.3 eV lower than that of the FM configuration. These observations indicate that while both FM and PM states favor distorted structures over the cubic phase, the FM state stabilizes the distorted phases more effectively, whereas the PM state provides greater stability to the ordered cubic structure.

To further investigate the role of structural distortion in the presence of oxygen vacancies, we analyze the total energy of vacancy-containing systems as a function of B-O-B bond angle distortion, as shown in Figure 4. We compute the total energy in three distinct ways: first, the ordered structure without relaxation (space group $Cmm2$), second, the ordered structure with relaxation (space group $Cmm2$), and third, the distorted structure with relaxation in no symmetry (space group $P1$). In the three structures, the distortion increases from the first to the last. From the data points, we observe that the total energy decreases as the distortion increases, indicating that structural distortions stabilize the system in the presence of oxygen vacancies.

In addition to the system energy, we illustrate the oxygen vacancy formation energies in Figure 4. For the distorted structure, the vacancy formation energy is approximately 1.2 eV. On the other hand, when using the pristine ordered structure (space group $Fm\bar{3}m$) as a reference, the vacancy formation energy in a symmetry-preserved system (space group $Cmm2$) is notably reduced to around 0.4 eV, demonstrating the strong influence of structural distortions on defect energetics. Fur-

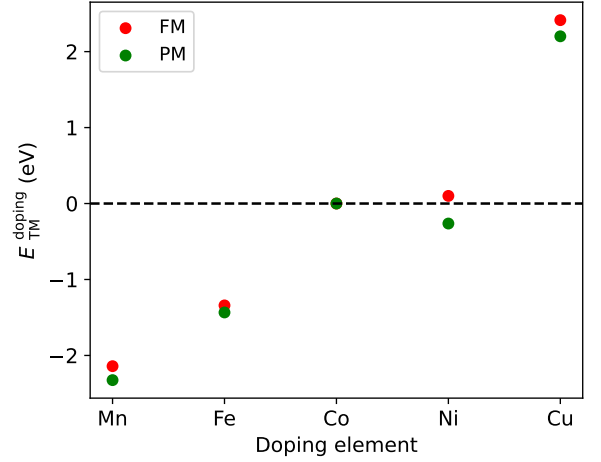


FIG. 5: Doping energy of pristine LSC with transition metal dopants (Mn, Fe, Ni, Cu) substituting a single Co atom. Red and green circles denote ferromagnetic (FM) and paramagnetic (PM) configurations, respectively. In both magnetic states, the formation energy of pure LSC, indicated by Co, was set to be zero as the reference.

thermore, a non-relaxed ordered structure yields a vacancy formation energy of approximately 1.4 eV, similar to the value obtained for the distorted system. However, this result is unrealistic since oxygen vacancy defects inevitably induce local structural relaxations. Therefore, in subsequent calculations, we consider only the vacancy formation energy obtained from the structurally distorted configurations.

B. Oxygen vacancies in doped LSC

In order to study the effects of dopant elements on the formation energy of oxygen vacancies, an initial investigation of the formation energy of substituting a single Co atom with TM dopants (Mn, Fe, Ni, Cu) in the pristine LSC crystal is conducted. We then calculate the formation energy of oxygen vacancies in the investigated material systems.

Figure 5 illustrates the TM-doping energies under FM and PM states. A clear correlation is observed between the TM doping energy trends in FM state, suggesting that the stability of doped LSC is governed by the intrinsic oxidation energies of the dopants. This trend is similar to the reported oxide formation energies of the dopant elements [42]. The doping energies in the PM state exhibit a slight reduction (0.1–0.3 eV) compared to those in the FM state across all dopants. However, this difference does not alter the overall energetic trend, which follows the sequence $\text{Mn} < \text{Fe} < \text{Co} < \text{Cu}$. The consistent trend implies that magnetic ordering barely affects the relative stability of dopants.

The only outlier is Ni dopant. The Ni dopant main-

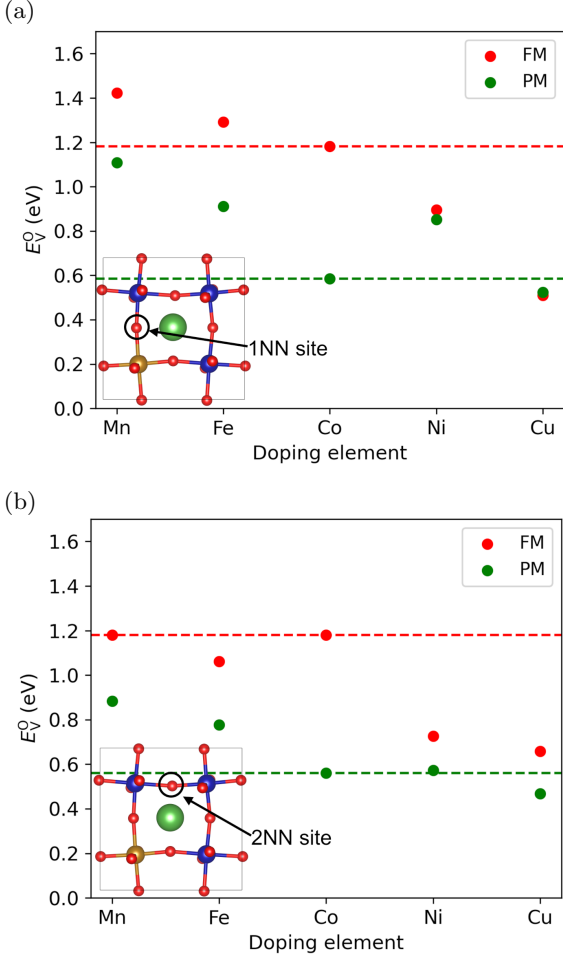


FIG. 6: Oxygen vacancy formation energy (a) at the 1NN and (b) at the 2NN sites of the doped LSC. FM and PM configurations are shown in red and green, respectively. For better comparison, the dashed lines mark E_V^O for the Co.

tains the doping energy trend in the FM configuration, consistent with its strong tendency to form stable oxides. However, its energy reduction in the PM state (~ 0.3 eV) is slightly larger than that of other dopants, leading to enhanced stability than pure LSC. This phenomenon is analogous to observations in other Ni-based perovskite systems, where the material has a tendency to stabilize PM or anti-FM states at low temperature [43].

We then investigate E_V^O in doped LSC depending on the magnetic states. Figure 6 compares E_V^O for first-nearest-neighbor (1NN) and second-nearest-neighbor (2NN) vacancy sites relative to the dopant site, respectively.

First, we investigate the effect of vacancy position on their formation energies. The doping elements affect not only the O atoms with which they form chemical bonds, but also the other O atoms by affecting the neighboring Co atoms. In the presence of TM dopants, differences in

the formation energies of two different oxygen vacancy sites have been observed. These variations can even alter the relative stability (compare the E_V^O in pure LSC) of the vacancies. Therefore, it is essential to consider both vacancy sites to understand the dopant-induced effects on the stability of the vacancies.

Next, we compare the vacancy formation energy between the FM and PM state. The PM state lowers E_V^O (compared to FM) for both 1NN and 2NN sites in most of the situations, which suggests that the PM state weakens the strength of TM-O bonds. This weakening is most pronounced in the pure LSC, resulting in an energy difference of 0.6 eV (difference between the dashed lines in Figure 6). For Fe and Mn dopants, this energy difference ranges from 0.3 eV to 0.4 eV. However, the situation becomes a bit more complicated for Ni and Cu doping. The vacancy formation energy remains largely unaltered at the 1NN vacancy nearest the doping site. In contrast, the formation energy of the 2NN vacancy is reduced by around 0.2 eV.

Vacancy positions and magnetic states together create even more complex variations in oxygen vacancy stability, with the effects of Fe and Ni dopants being particularly pronounced. For the 1NN vacancy, the Fe-doped FM state exhibits a higher vacancy formation energy compared to the LSC. However, this tendency is reversed at the 2NN site. In contrast, for the PM state, the Fe-doped system exhibits higher vacancy formation energies than the LSC for both vacancy positions. For Ni doping, the vacancy formation energy is consistently lower in the FM state than in the LSC, while in the PM state, the vacancy formation energy is always higher than its formation energy in the LSC. Consequently, the energy change induced by the PM magnetic state qualitatively affects stability of the oxygen vacancy in the doped system.

To further elucidate the interplay between defects and magnetic states, Figure 7 quantifies the energy difference between the two magnetic states ($\Delta E_{\text{FM-PM}}$) for the crystals with and without oxygen vacancy. The results demonstrate an absence of regularity in the apparent changes in $\Delta E_{\text{FM-PM}}$.

Specifically, the introduction of an oxygen vacancy alters $\Delta E_{\text{FM-PM}}$ in a dopant-dependent manner, suggesting that local structural and electronic rearrangements around the vacancy site significantly influence spin alignment preferences. The most pronounced change in $\Delta E_{\text{FM-PM}}$ due to oxygen vacancy formation is observed in pristine LSC, where the energy difference decreases by approximately 0.5 eV. In contrast, Mn- and Fe-doped systems exhibit a more moderate reduction in $\Delta E_{\text{FM-PM}}$, with values decreasing by around 0.35 eV. On the other hand, for Ni and Cu doping, the energy difference remains largely unchanged regardless of the presence or absence of an oxygen vacancy, indicating a weaker dependency between defect formation and magnetic stability in these systems.

The results of this section illustrate the interplay

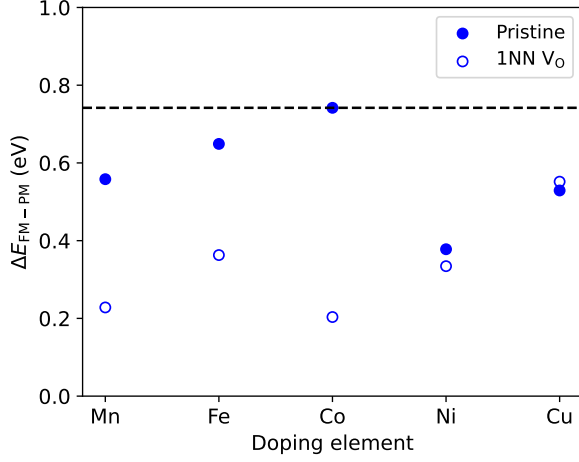


FIG. 7: Energy difference between PM and FM states ($\Delta E_{\text{FM-PM}}$) for pristine crystals and crystals with 1NN V_{O} , denoted as solid and open markers, respectively.

among doping chemistry, oxygen vacancy defects, and magnetic order. However, these relationships do not exhibit a uniform trend. In particular, while our aim is to qualitatively elucidate the relationship between oxygen vacancy formation energy and magnetic order, significant variations are observed across different compositional systems. Attempts to correlate these variations with crystallographic parameters—such as TM-O bond lengths, bond angles, and ionic radii—were unsuccessful. Consequently, our calculations indicate that there is a complex interplay of different factors, and it is necessary to investigate the electronic structure of the systems.

C. Electronic structure analysis

In order to assess the doping-induced modifications in the electronic structure of LSC, we conduct a comparative analysis of the projected density of states (pDOS) for the doped crystals. The pDOS of crystals without V_{O} are compared between the FM and PM states. For the sake of clarity, the contributions from La and Sr elements had been omitted from the figures.

Figure 8 illustrates the detailed information of the pDOS. The band center, as the famous effective electronic descriptor [44], is also labeled in the figure. The band center is defined as the energy-weighted average of the orbital, i.e., $\varepsilon_{\text{center}} = \frac{\int E \cdot D(E) dE}{\int D(E) dE}$ [45]. Across all dopants, the overall energy landscape remains qualitatively similar, indicating that the fundamental B-O bonding framework is preserved. This suggests that substituting different TM elements at the B-site does not introduce drastic modifications to the hybridization between O $2p$ and TM $3d$ orbitals. However, the energy difference between the center of the O $2p$ band and TM $3d$ band (ΔE_{cen}) is affected by the dopants and the mag-

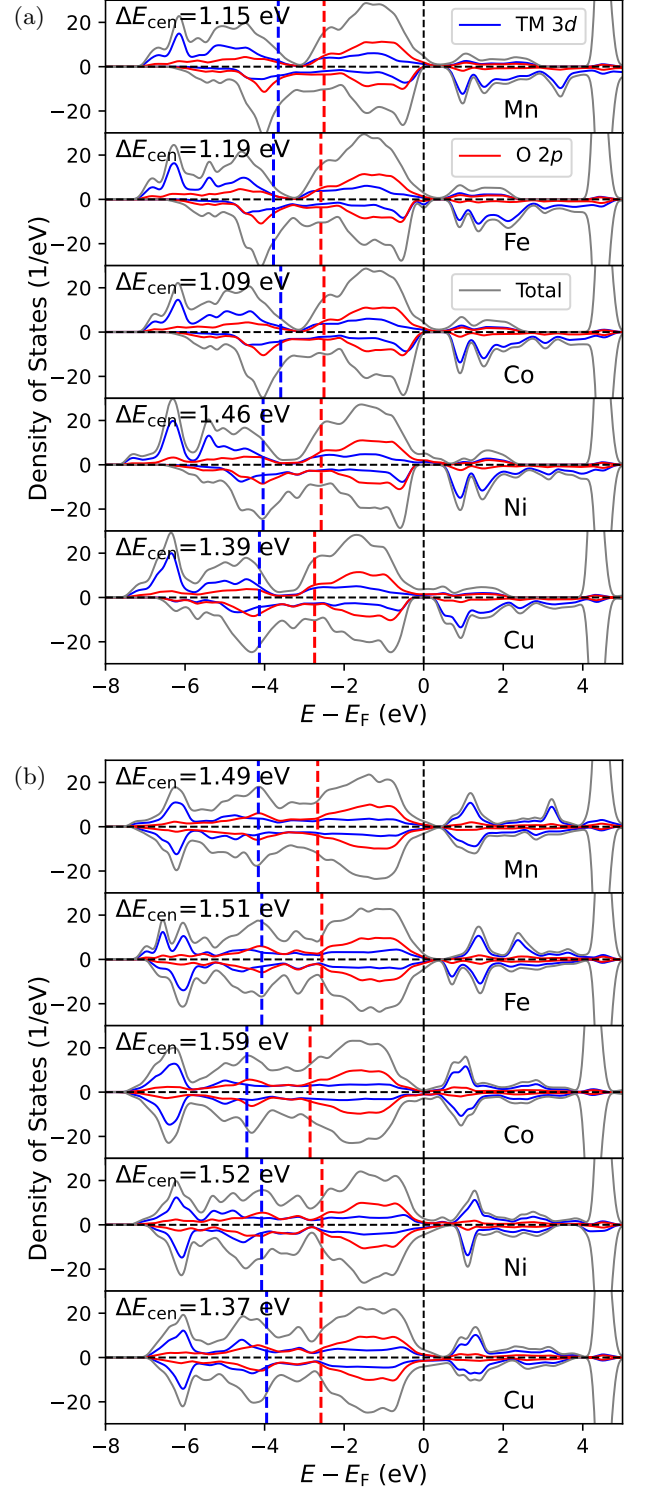


FIG. 8: Projected density of states for doped LSC of (a) the FM state and (b) the PM state. Each panel displays the TM $3d$ orbital (blue), the O $2p$ orbital (red), and the total density of states (gray), with energies referenced to the Fermi level (E_{F}). Spin-up and spin-down data are shown in each upper and lower panel, respectively. Vertical dashed lines denote the band centers of the occupied O $2p$ (red) and TM $3d$ (blue) states, and ΔE_{cen} is the energy difference between the two centers.

netic states. For the FM state, Mn and Fe dopants maintain a similar ΔE_{cen} to LSC, while the Ni and Cu dopants expand it by 0.37 and 0.30 eV, respectively. In contrast, Mn, Fe, and Ni dopants in the PM state show a similar ΔE_{cen} , while the Cu dopant decreases the ΔE_{cen} around 0.2 eV.

Furthermore, the change in ΔE_{cen} between the two magnetic states is also related to the type of dopants. Specifically, as the magnetic state transitions from FM to PM state, the ΔE_{cen} increases by 0.5 eV within a pure LSC crystal. The increase for Mn and Fe dopants is slightly less than that for LSC, 0.34 and 0.32 eV, respectively. The Ni and Cu dopants exhibit a comparatively negligible change below 0.1 eV.

In summary, our pDOS analysis reveals that, while the overall energy landscapes of the TM $3d$ and O $2p$ states remain qualitatively similar across all dopants, indicating that the fundamental B–O bonding framework is preserved, the band centers exhibit modifications that are dopant- and magnetic state-dependent. These results underscore the complex interplay between dopant chemistry and magnetic states in modulating the electronic structure of LSC.

IV. DISCUSSION

In this study, we presented the critical role of structural distortions in stabilizing the LSC system and modulating the formation energy of oxygen vacancies. Our findings are consistent with previous studies that have highlighted the significance of J-T distortions and octahedral tilting in transition metal oxides [26, 46]. Specifically, we observe that the cubic phase of LSC corresponds to a local energy maximum due to its inherent instability, whereas distorted structures are energetically favored, as illustrated in Figure 3. This behavior is well-documented in perovskite oxides, where cooperative J-T distortions lower the total energy and enhance the structural stability [47].

The comparison between the FM and PM states under the conditions of structural distortion further reveals intriguing stability trends. While both FM and PM states exhibit a preference for distorted structures over the ordered cubic phase, the FM state stabilizes the distorted structures more effectively. This observation is supported by prior theoretical investigations of transition metal perovskites, which indicate that magnetic ordering can influence the energy landscape by coupling to structural distortions [26, 48]. Furthermore, the stability of the magnetic state is found to be contingent upon the distortion angles, suggesting a sensitivity of the magnetic state to the structural parameters. This sensitivity of the magnetic state to structural distortions is further substantiated by Woicik *et al.*, who observed a change in the Curie temperature of LSC films under different strains [23].

Our analysis of oxygen vacancy formation energies also reveals a significant dependence on the structural distortion,

cf. Fig. 4. When considering the most stable distorted structure, the vacancy formation energy is approximately 1.2 eV. While, if the ordered structure is used as a reference, the vacancy formation energy is drastically reduced to around 0.4 eV. Several previous studies on oxygen-deficient perovskites have emphasized the importance of lattice distortion too, showing that neglecting it leads to substantial underestimation of vacancy formation energies [49, 50]. More specifically, the research conducted by Baldassarri *et al.* [49] has indicated an energy underestimation of about 1 eV per oxygen vacancy for perovskite crystals, is in close agreement with our result. Consequently, our findings reinforce the need to incorporate structural distortions in defect calculations to obtain reliable energetic estimates.

We then analyzed the crystal structural distortion caused by the dopants. However, we did not find significant changes in bond angle and bond length during element substitution. Here we use the average bond angle because TM-O octahedra are always influenced by neighboring octahedra. We compared the effect of dopants on the bond angles for pristine crystals, crystals with V_{O} , and the same magnetic state, respectively. Compared to pure LSC, the average bond angle change in these cases for doped LSC is always in 1° . Therefore, we suggest that the energy changes due to crystal structure changes caused by these dopants can be neglected. Instead, these energy variations are attributable to the oxidizability of the dopants themselves, as well as to differences in response of the dopants to different magnetic states.

The difference of E_{V}^{O} between the two magnetic states can be qualitatively explained by the double exchange interaction. The O atom between the two TM atoms is suggested to act as a bridge for double exchange in a FM perovskite oxide [51]. The presence of V_{O} diminishes the bridge, thereby increasing the energy of the entire system. Consequently, the E_{V}^{O} is expected to be higher in the FM state compared to the PM state. However, as illustrated in Figure 6, the E_{V}^{O} in FM and PM for Ni and Cu dopants are comparable, suggesting that Ni and Cu interrupt the double exchange before the presence of V_{O} . This indicates that the low spin of Ni and Cu dopants hinder the double exchange. A similar phenomenon was reported by Mizokawa *et al.* [26], who indicated that the low-spin Ni and Cu compounds in perovskites weaken the double exchange, which in turn destabilizes spin ordering.

The hypothesis of defect effects on the double exchange mechanism can also provide a qualitative framework for understanding their influence on the magnetic ordering temperature in LSC. Experimental studies by Baskar *et al.* [31] have shown that the presence of oxygen vacancies in LSC leads to a reduction in the magnetic ordering temperature compared to the pristine crystal. This observed decrease can be attributed to a reduction in the energy difference between the PM and FM states, a trend consistent with the results presented in Figure 7 (Co, Mn and Fe). Specifically, the suppression of the double-exchange mechanism, caused by oxygen vacancies, de-

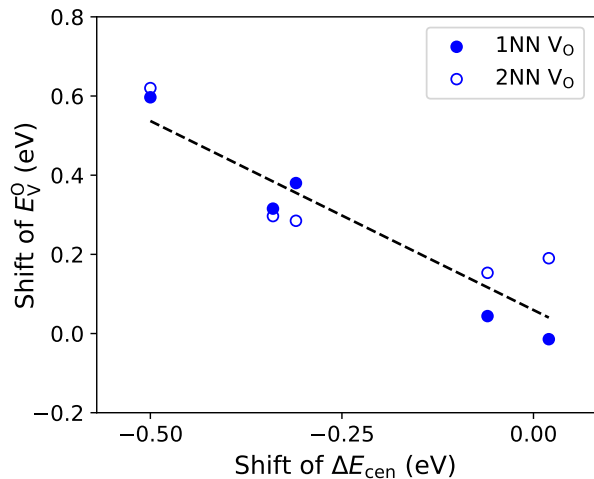


FIG. 9: Scatter plot of the energy difference between O $2p$ and TM $3d$ band centers versus the energy difference between FM and PM states in doped LSC. Solid and open blue circles denote the two different oxygen vacancies. The dashed line is the linear fitting of all data points.

creases the relative stability of the ferromagnetic state, thereby lowering the magnetic ordering temperature. In contrast, for low-spin dopants, such as Ni and Cu, the presence or absence of V_O has little effect on the relative stability of the two magnetic states in the doped LSC. In this case, the roles of oxygen vacancies and low-spin dopants in hindering the double exchange interaction are consistent.

To understand the different trends of double exchange interactions under various doping elements, we analyzed the electronic structure. The double exchange interaction exerts a significant influence on the distribution of electrons [52, 53], and this phenomenon can be observed in the pDOS. Stronger double exchange increases the degree of orbital overlap and the strength of chemical bond [54], which in turn affects the corresponding band center distances. In the energy range under consideration, the density of states is predominantly governed by contributions from the B-site TM $3d$ orbitals (including both t_{2g} and e_g components) and O $2p$ orbitals. The occupied state centers of the O $2p$ and TM $3d$ bands are labeled in Figure 8. In this figure, we provide data for two magnetic states, FM and PM, for comparison. Note that the band center is calculated under the conditions of pristine crystals without V_O . We expect to correlate the variations between them with the trends of E_V^O in different doping systems.

Figure 9 illustrates the relationship between the shift of ΔE_{cen} and the shift of E_V^O . These shifts arise from the difference between FM and PM states (FM minus PM). The band center takes into account the combined effects of the properties of the elements themselves and the double exchange interactions. We refrain to label the elements in this figure, as all systems should conform to

our hypothesis. All the data points form an approximate linear relationship.

This linear relationship confirms our earlier hypothesis that defects influence double exchange interactions. The doping elements partially obstruct the double exchange interaction, whereas the presence of V_O is likely to completely obstruct them. When the doping elements fully obstruct the double exchange interactions, there is little change in the shift of E_V^O , corresponding to the right part of the line. Conversely, when the doping elements do not fully hinder double exchange interactions, the V_O takes responsibility for hindering the remaining double exchange interactions, thus increasing E_V^O , which corresponds to the left part of the line. Therefore, the influence of doping elements on E_V^O exhibits inconsistent trends under different magnetic states, and this inconsistency is determined by the varying degrees of hindrance that defects impose on double exchange interactions.

V. SUMMARY

In this study, we utilized DFT calculations to systematically explore the effects of $3d$ transition-metal doping on the oxygen vacancy formation energies in the LSC perovskite material. Two magnetic orders were considered to uncover the intricate relationships among dopant chemistry, magnetic order, and defect energetics. Our results reveal that the formation energies of oxygen vacancies in the doped LSC are strongly influenced by both the magnetic state of the system and the choice of $3d$ transition-metal dopant. The PM state, which serves as a model for general operational conditions, exhibits a different trend of oxygen vacancy formation energies when compared to the FM ground state. This difference cannot be quantitatively analyzed in terms of pristine crystal structure alteration and oxidizability of the doped elements. Utilizing the ground state FM to assess the oxygen vacancy formation energies of a doped system may lead to qualitative inaccuracies. The reason for this inaccuracy is the effect of the doping element on the double exchange interaction, as we discussed in Fig. 9. This emphasizes the need to account for magnetic disorder in computational studies. These findings lay the foundation for the development of customized perovskite materials with enhanced performance in electrochemical applications, such as SOFCs and oxygen separation membranes, where precise control over oxygen vacancy concentrations is paramount.

ACKNOWLEDGMENTS

This work was funded by the European Union under Grant Agreement 101080142, as part of the EQUALITY project. The authors thank David David (Capgemini SE) for fruitful discussions. The work was enabled in part by the Nextsim HPC at Chemnitz University of Technology.

- [1] A. D. Poletayev, J. A. Dawson, M. S. Islam, and A. M. Lindenberg, Defect-driven anomalous transport in fast-ion conducting solid electrolytes, *Nature Materials* **21**, 1066 (2022).
- [2] Z. Shao and S. M. Haile, A high-performance cathode for the next generation of solid-oxide fuel cells, *Nature* **431**, 170 (2004).
- [3] B. C. Steele and A. Heinzel, Materials for fuel-cell technologies, *Nature* **414**, 345 (2001).
- [4] M. Mogensen, D. Lybye, N. Bonanos, P. Hendriksen, and F. Poulsen, Factors controlling the oxide ion conductivity of fluorite and perovskite structured oxides, *Solid State Ionics* **174**, 279 (2004).
- [5] A. Orera and P. Slater, New chemical systems for solid oxide fuel cells, *Chemistry of Materials* **22**, 675 (2010).
- [6] C. Sun, J. A. Alonso, and J. Bian, Recent advances in perovskite-type oxides for energy conversion and storage applications, *Advanced Energy Materials* **11**, 2000459 (2021).
- [7] J. A. Kilner, Fast oxygen transport in acceptor doped oxides, *Solid State Ionics* **129**, 13 (2000).
- [8] S. J. Skinner and J. A. Kilner, Oxygen ion conductors, *Materials Today* **6**, 30 (2003).
- [9] D. Lee, Y.-L. Lee, W. T. Hong, M. D. Biegalski, D. Morgan, and Y. Shao-Horn, Oxygen surface exchange kinetics and stability of $(\text{La}, \text{Sr})_2\text{CoO}_{4\pm\delta}/\text{La}_{1-x}\text{Sr}_x\text{MO}_{3-\delta}$ ($\text{M} = \text{Co}$ and Fe) hetero-interfaces at intermediate temperatures, *Journal of Materials Chemistry A* **3**, 2144 (2015).
- [10] E. D. Wachsman and K. T. Lee, Lowering the temperature of solid oxide fuel cells, *Science* **334**, 935 (2011).
- [11] S. B. Adler, Factors governing oxygen reduction in solid oxide fuel cell cathodes, *Chemical Reviews* **104**, 4791 (2004).
- [12] J. Cheng, P. Ganesan, Z. Wang, M. Zhang, G. Zhang, N. Maeda, J. Matsuda, M. Yamauchi, B. Chi, and N. Nakashima, Bifunctional electrochemical properties of $\text{La}_{0.8}\text{Sr}_{0.2}\text{Co}_{0.8}\text{M}_{0.2}\text{O}_{3-\delta}$ ($\text{M} = \text{Ni}, \text{Fe}, \text{Mn}, \text{and Cu}$): efficient elemental doping based on a structural and ph-dependent study, *Materials Advances* **3**, 272 (2022).
- [13] D. Mantzavinos, A. Hartley, I. S. Metcalfe, and M. Sahibzada, Oxygen stoichiometries in $\text{La}_{1-x}\text{Sr}_x\text{Co}_{1-y}\text{Fe}_y\text{O}_{3-\delta}$ perovskites at reduced oxygen partial pressures, *Solid State Ionics* **134**, 103 (2000).
- [14] S. Ingavale, M. Gopalakrishnan, C. M. Enoch, C. Pornrungrroj, M. Rittirum, S. Praserttham, A. Somwangthanaroj, K. Nootong, R. Pornprasertsuk, and S. Kheawhom, Strategic design and insights into lanthanum and strontium perovskite oxides for oxygen reduction and oxygen evolution reactions, *Small* **20**, 2308443 (2024).
- [15] W. Jia, Y. Wang, J. Huang, M. Li, B. Xiang, Y. Wang, L. Wu, L. Zheng, and L. Ge, Alternative B-site-doped $\text{La}_{0.6}\text{Sr}_{0.4}\text{Co}_{0.2}\text{Fe}_{0.8-x}\text{M}_x\text{O}_3$ ($\text{M} = \text{Ni}, \text{Cu}, \text{Nb}; x = 0, 0.1, 0.2$) as innovative cathode material for LT-SOFC with enhanced charge transfer and oxygen ion diffusion, *Applied Energy* **353**, 122096 (2024).
- [16] H. Li, Z. Su, P. Zhang, F. Liu, C. Fan, L. Xu, G. Guo, and D. Zhang, A first-principles investigation of the effects of strain and Pd-doping on ion transfer in LSCF bulk of solid oxide cells, *Computational Materials Science* **227**, 112276 (2023).
- [17] T. Jia, J. W. Lekse, G. A. Hackett, and Y. Duan, Effects of site and magnetic disorder on the oxygen vacancy formation and electronic and optical properties of $\text{La}_x\text{Sr}_{1-x}\text{CoO}_{3-\delta}$ and $\text{SrFe}_y\text{Co}_{1-y}\text{O}_{3-\delta}$, *The Journal of Physical Chemistry C* **125**, 12374 (2021).
- [18] M. Senaris-Rodriguez and J. Goodenough, Magnetic and transport properties of the system $\text{La}_{1-x}\text{Sr}_x\text{CoO}_{3-\delta}$ ($0 \leq x \leq 0.50$), *Journal of Solid State Chemistry* **118**, 323 (1995).
- [19] V. Bhide, D. Rajoria, C. Rao, G. R. Rao, and V. Jadhao, Itinerant-electron ferromagnetism in $\text{La}_{1-x}\text{Sr}_x\text{CoO}_3$: A Mössbauer study, *Physical Review B* **12**, 2832 (1975).
- [20] J. Meng, N. Yuan, X. Liu, C. Yao, Q. Liang, D. Zhou, F. Meng, and J. Meng, Synergistic effects of intrinsic cation disorder and electron-deficient substitution on ion and electron conductivity in $\text{La}_{1-x}\text{Sr}_x\text{Co}_{0.5}\text{Mn}_{0.5}\text{O}_{3-\delta}$ ($x = 0, 0.5$, and 0.75), *Inorganic Chemistry* **54**, 2820 (2015).
- [21] M. Pavone, A. B. Munoz-Garcia, A. M. Ritzmann, and E. A. Carter, First-principles study of lanthanum strontium manganite: Insights into electronic structure and oxygen vacancy formation, *The Journal of Physical Chemistry C* **118**, 13346 (2014).
- [22] J. Walter, G. Yu, B. Yu, A. Grutter, B. Kirby, J. Borchers, Z. Zhang, H. Zhou, T. Birol, M. Greven, *et al.*, Ion-gel-gating-induced oxygen vacancy formation in epitaxial $\text{La}_{0.5}\text{Sr}_{0.5}\text{CoO}_{3-\delta}$ films from in operando X-ray and neutron scattering, *Physical Review Materials* **1**, 071403 (2017).
- [23] J. Woicik, C. Xie, and B. Wells, Effect of strain on the local perovskite structure: $\text{La}_{0.5}\text{Sr}_{0.5}\text{CoO}_3$, *Journal of Applied Physics* **109** (2011).
- [24] M. Kubicek, Z. Cai, W. Ma, B. Yildiz, H. Hutter, and J. Fleig, Tensile lattice strain accelerates oxygen surface exchange and diffusion in $\text{La}_{1-x}\text{Sr}_x\text{CoO}_{3-\delta}$ thin films, *ACS Nano* **7**, 3276 (2013).
- [25] B. Kamecki, J. Karczewski, P. Jasiński, and S. Molin, Improvement of oxygen electrode performance of intermediate temperature solid oxide cells by spray pyrolysis deposited active layers, *Advanced Materials Interfaces* **8**, 2002227 (2021).
- [26] T. Mizokawa and A. Fujimori, Unrestricted hartree-fock study of transition-metal oxides: Spin and orbital ordering in perovskite-type lattice, *Physical Review B* **51**, 12880 (1995).
- [27] A. Rata, A. Herklotz, K. Nenkov, L. Schultz, and K. Dörr, Strain-induced insulator state and giant gauge factor of $\text{La}_{0.7}\text{Sr}_{0.3}\text{CoO}_3$ films, *Physical Review Letters* **100**, 076401 (2008).
- [28] Z. Cai, Y. Kuru, J. W. Han, Y. Chen, and B. Yildiz, Surface electronic structure transitions at high temperature on perovskite oxides: the case of strained $\text{La}_{0.8}\text{Sr}_{0.2}\text{CoO}_3$ thin films, *Journal of the American Chemical Society* **133**, 17696 (2011).
- [29] D. Louca, J. L. Sarrao, J. D. Thompson, H. Röder, and G. Kwei, Correlation of local Jahn-Teller distortions to the magnetic/conductive states of $\text{La}_{1-x}\text{Sr}_x\text{CoO}_3$, *Physical Review B* **60**, 10378 (1999).
- [30] R. Mandal, Y. Mahton, C. Sowjanya, K. Sanket, S. K. Behera, and S. K. Pratihari, Electrocatalytic behaviour

- of Cu-substituted $\text{La}_{0.5}\text{Sr}_{0.5}\text{Co}_{0.8}\text{Fe}_{0.2-x}\text{Cu}_x\text{O}_{3-\delta}$ ($x=0-0.2$) perovskite oxides, *Journal of Solid State Chemistry* **317**, 123668 (2023).
- [31] D. Baskar and S. B. Adler, High temperature magnetic properties of sr-doped lanthanum cobalt oxide ($\text{La}_{1-x}\text{Sr}_x\text{CoO}_{3-\delta}$), *Chemistry of Materials* **20**, 2624 (2008).
- [32] B. Alling, T. Marten, and I. Abrikosov, Effect of magnetic disorder and strong electron correlations on the thermodynamics of CrN, *Physical Review B—Condensed Matter and Materials Physics* **82**, 184430 (2010).
- [33] M. E. Merkel, A. M. Tehrani, and C. Ederer, Probing the mott insulating behavior of $\text{Ba}_2\text{MgReO}_6$ with DFT+DMFT, *Physical Review Research* **6**, 023233 (2024).
- [34] S. Yoon, K. Jin, S. Lee, K. T. Nam, M. Kim, and Y.-K. Kwon, Effects of paramagnetic fluctuations on the thermochemistry of MnO (100) surfaces in the oxygen evolution reaction, *Physical Chemistry Chemical Physics* **23**, 859 (2021).
- [35] N. Golosova, D. Kozlenko, L. Dubrovinsky, V. Cerantola, M. Bykov, E. Bykova, S. Kichanov, E. V. Lukin, B. Savenko, A. V. Ponomareva, *et al.*, Magnetic and structural properties of FeCO_3 at high pressures, *Physical Review B* **96**, 134405 (2017).
- [36] G. Kresse and J. Furthmüller, Efficiency of ab-initio total energy calculations for metals and semiconductors using a plane-wave basis set, *Computational Materials Science* **6**, 15 (1996).
- [37] P. E. Blöchl, Projector augmented-wave method, *Physical Review B* **50**, 17953 (1994).
- [38] J. P. Perdew, K. Burke, and M. Ernzerhof, Generalized gradient approximation made simple, *Physical Review Letters* **77**, 3865 (1996).
- [39] S. L. Dudarev, G. A. Botton, S. Y. Savrasov, C. Humphreys, and A. P. Sutton, Electron-energy-loss spectra and the structural stability of nickel oxide: An LSDA+U study, *Physical Review B* **57**, 1505 (1998).
- [40] H. J. Monkhorst and J. D. Pack, Special points for brillouin-zone integrations, *Physical Review B* **13**, 5188 (1976).
- [41] E. Bitzek, P. Koskinen, F. Gähler, M. Moseler, and P. Gumbsch, Structural relaxation made simple, *Physical Review Letters* **97**, 170201 (2006).
- [42] L. Wang, T. Maxisch, and G. Ceder, Oxidation energies of transition metal oxides within the GGA+U framework, *Physical Review B—Condensed Matter and Materials Physics* **73**, 195107 (2006).
- [43] A. Zunger and O. I. Malyi, Understanding doping of quantum materials, *Chemical Reviews* **121**, 3031 (2021).
- [44] B. Hammer and J. K. Norskov, Why gold is the noblest of all the metals, *Nature* **376**, 238 (1995).
- [45] F. Ando, T. Gunji, T. Tanabe, I. Fukano, H. D. Abruna, J. Wu, T. Ohsaka, and F. Matsumoto, Enhancement of the oxygen reduction reaction activity of Pt by tuning its d-band center via transition metal oxide support interactions, *ACS Catalysis* **11**, 9317 (2021).
- [46] P. V. Balachandran and J. M. Rondinelli, Interplay of octahedral rotations and breathing distortions in charge-ordering perovskite oxides, *Physical Review B—Condensed Matter and Materials Physics* **88**, 054101 (2013).
- [47] J. M. Rondinelli and N. A. Spaldin, Structure and properties of functional oxide thin films: insights from electronic-structure calculations, *Advanced Materials* **23**, 3363 (2011).
- [48] D. Phelan, D. Louca, S. Rosenkranz, S.-H. Lee, Y. Qiu, P. Chupas, R. Osborn, H. Zheng, J. Mitchell, J. Copley, *et al.*, Nanomagnetic droplets and implications to orbital ordering in $\text{La}_{1-x}\text{Sr}_x\text{CoO}_3$, *Physical Review Letters* **96**, 027201 (2006).
- [49] B. Baldassarri, J. He, X. Qian, E. Mastronardo, S. Griesemer, S. M. Haile, and C. Wolverton, Accuracy of DFT computed oxygen-vacancy formation energies and high-throughput search of solar thermochemical water-splitting compounds, *Physical Review Materials* **7**, 065403 (2023).
- [50] Y. Wang, B. Baldassarri, J. Shen, J. He, and C. Wolverton, Landscape of thermodynamic stabilities of $\text{A}_2\text{BB}'\text{O}_6$ compounds, *Chemistry of Materials* **36**, 6816 (2024).
- [51] P. W. Anderson and H. Hasegawa, Considerations on double exchange, *Physical Review* **100**, 675 (1955).
- [52] O. N. Meetei, O. Erten, A. Mukherjee, M. Randeria, N. Trivedi, and P. Woodward, Theory of half-metallic double perovskites. I. double exchange mechanism, *Physical Review B—Condensed Matter and Materials Physics* **87**, 165104 (2013).
- [53] O. Erten, O. N. Meetei, A. Mukherjee, M. Randeria, N. Trivedi, and P. Woodward, Theory of half-metallic double perovskites. II. effective spin hamiltonian and disorder effects, *Physical Review B—Condensed Matter and Materials Physics* **87**, 165105 (2013).
- [54] W. Lv, F. Krüger, and P. Phillips, Orbital ordering and unfrustrated $(\pi, 0)$ magnetism from degenerate double exchange in the iron pnictides, *Physical Review B—Condensed Matter and Materials Physics* **82**, 045125 (2010).